Recent advancements towards large-scale flow diagnostics by robotic PIV

Scarano, Fulvio; Jux, Constantin; Sciacchitano, Andrea

DOI
10.1088/1873-7005/abe034

Publication date
2021

Document Version
Final published version

Published in
Fluid Dynamics Research

Citation (APA)
Scarano, F., Jux, C., & Sciacchitano, A. (2021). Recent advancements towards large-scale flow diagnostics by robotic PIV. *Fluid Dynamics Research*, *53*(1), Article 011401. https://doi.org/10.1088/1873-7005/abe034

Fluid Dynamics Research

Recent advancements towards large-scale flow diagnostics by robotic PIV

To cite this article: Fulvio Scarano *et al* 2021 *Fluid Dyn. Res.* **53** 011401

IOP Publishing | The Japan Society of Fluid Mechanics Fluid Dynamics Research

Fluid Dyn. Res. **53** (2021) 011401 (13pp) https://doi.org/10.1088/1873-7005/abe034

Recent advancements towards large-scale flow diagnostics by robotic PIV

Fulvio Scarano, Constantin Jux and Andrea Sciacchitano

Department of Aerospace Engineering, TU Delft, Delft, The Netherlands

E-mail: f.scarano@tudelft.nl

Received 12 May 2019; revised 6 September 2020
Accepted for publication 26 January 2021
Published 17 February 2021

Communicated by Professor Yasuhide Fukumoto

Abstract

The present work reviews the recent developments in the domain of particle image velocimetry (PIV) with attention to its use for large-scale problems of interest for industrial aerodynamics. The article introduces the fundamental principles of flow seeding for large-scale experiments based on the helium-filled soap bubble (HFSB) technique. The measurement of flow tracers in a three-dimensional domain is presented, which is based on Lagrangian tracking methods. Furthermore, the concept of co-axial volumetric velocimetry is introduced and its combination with robotic arm manipulation is shown. The work presents two main examples of applications to aerodynamic problems: the first is the flow field around a propeller aircraft at wind tunnel free-stream velocity up to 50 m s^{-1}, which to date is considered the boundary of large-scale PIV application with HFSB. The second example is the complex three-dimensional flow field around a cyclist at full scale. The work summarizes developments obtained in the last 3 years of research, demonstrating that the domain of PIV techniques is still undergoing vivid developments.

Keywords: particle image velocimetry, aerodynamics, helium filled soap bubbles, large scale experiments, flow visualization

1. Introduction

The use of particle image velocimetry (PIV) among fluid dynamic research laboratories has become widespread due to its capabilities to render quantitative flow field data with high precision and spatial resolution. However, setting up the diagnostic system often remains a lengthy procedure, requiring specialized skills in the domain of precision mechanics, optics, and digital image analysis. The latter is often reported as the main reason delaying the diffusion of PIV among industry for testing.

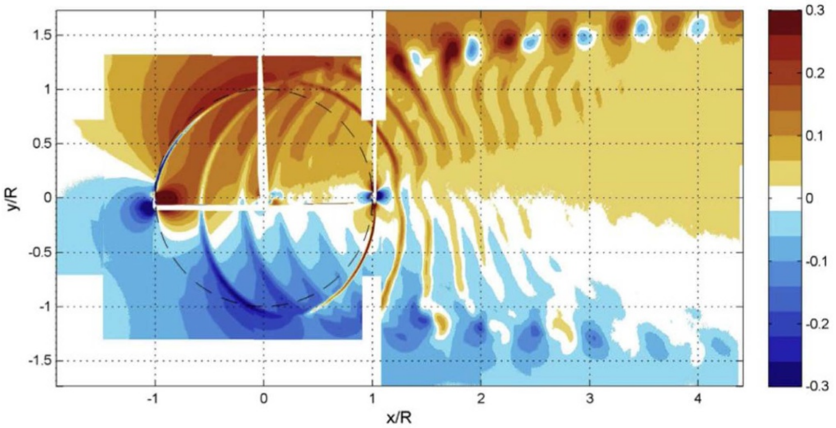

Figure 1. Large scale stereo-PIV measurements around a vertical axis wind turbine (contours of phase averaged spanwise velocity component. $R = 0.5$ m). Measurement patches of approximately 26×75 cm^2 (repr. from Tescione *et al* 2014).

A second major obstacle pertains the domain of aerodynamics, where the physical limits of the technique are often reached when attempting large-scale experiments (in the order of a meter or more). The use of micron-size droplets typically limits the planar measurement domain to 40×30 cm^2 (Raffel *et al* 2018). Significantly larger domains are therefore usually realized by combination of multiple measurement patches (e.g. Tescione *et al* 2014; figure 1).

Three-dimensional PIV measurements, for instance by tomographic PIV, have been limited to even smaller size (10–100 cm^3) due to the stringent requirements on camera aperture to achieve the necessary depth of focus (Scarano 2013).

2. Large-scale diagnostics

Experiments at large scale require that the measurement domain can be scaled up, making use of seeding tracers that scatter light more effectively than the currently adopted micrometric droplets (e.g. fog or oil) by orders of magnitude. Helium-filled soap bubbles (HFSB) of sub-millimeter diameter (200–800 μm) have been used for the PIV analysis over large domains (Bosbach *et al* 2009) and they were proven to scatter 10^4–10^5 more light than micron sized droplets (Caridi *et al* 2016). A schematic description of an HFSB generator is provided in figure 2.

The relation between the measurement volume V and particle image peak intensity I_p received by the camera system follows a law of type $I_\mathrm{p} \sim V^{-1}$ (when pixel size governs the particle image size). As a result, doubling the linear size of the measurement domain requires order of magnitude increase of the scattered light. The favorable ratio between the scattering of HFSB and micron-size particles, accommodates for order-of-magnitude increase of the measurement volume bringing it to the order of 10–100 l.

The development of HFSB seeding techniques for PIV in wind tunnels (figure 3) has started recently (Scarano *et al* 2015) and their ability to trace airflows with good fidelity has been demonstrated in the range of 10–30 m s^{-1}. Lately, HFSB tracers were demonstrated up to flow velocity of 50 m s^{-1} in turbulent shear flows (Engler Faleiros *et al* 2018, figure 4).

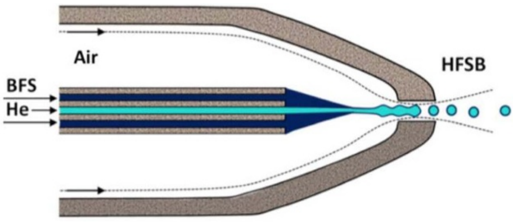

Figure 2. Schematic description of HFSB generation from concentric ducts and air flow nozzle (repr. from Engler Faleiros *et al* 2018).

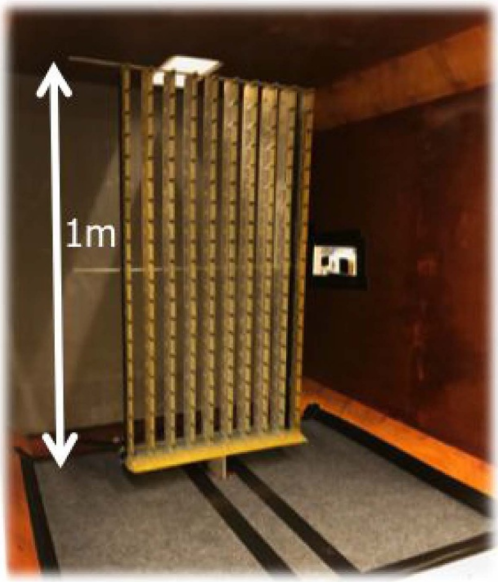

Figure 3. Aerodynamically shaped HFSB generation system (200 bubble generators in parallel) for use in the wind tunnel settling chamber.

The second, not less important, requirement is a rapid adjustment of the measurement system when the domain of interest needs to be covered by several views. Three-dimensional techniques like tomographic PIV (Elsinga *et al* 2006), 3D particle tracking velocimetry (PTV, Murai *et al* 2007) or scanning light sheet (Bruecker 1997) require a careful placement and calibration of the apparatus before measurements can be performed. It is commonly reported that the procedure can take a few hours to a day. Most of the time is spent in the setting of the multiple cameras' fields of view, focal range, Scheimpflug condition and mutual positioning estimation by *in-situ* calibrations.

A compact arrangement of imagers and illumination circumvents the above steps when the region of interest needs to be moved around a complex three-dimensional object. A system where the mutual position among imagers is kept constant, along with their relation to the illumination system, can be repositioned in physical space avoiding the lengthy procedures of alignment and calibration. This is achieved with the concept of coaxial volumetric

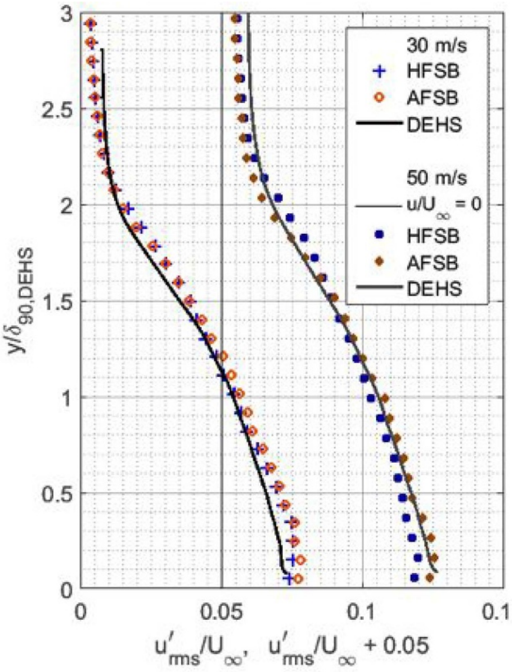

Figure 4. Streamwise velocity fluctuations in a turbulent boundary layer. Measurements with HFSB are compared to micron-size seeding (DEHS (di-ethyl-hexyl-sebacat)) at 30 and 50 m s^{-1}. (AFSB stands for air-filled soap bubbles, which are slightly heavier than air.) (repr. from Engler Faleiros *et al* 2018).

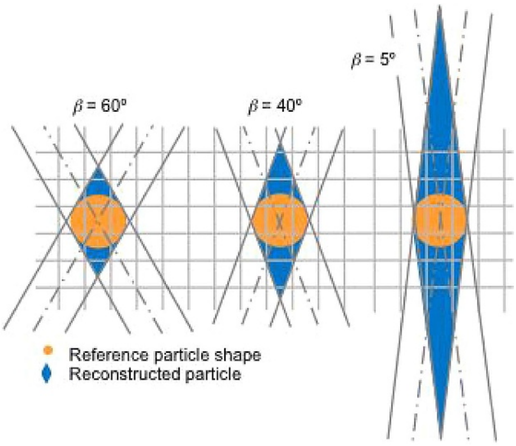

Figure 5. Reconstructed particles in 3D space and axial uncertainty as a function of the tomographic aperture β.

velocimetry (CVV, Schneiders *et al* 2018; figure 5) whereby a low-aperture (4–6°) tomographic imaging system is coupled with conical illumination from the same (coaxial) direction as the lines of sight to realize 3D (volumetric) measurements. CMOS (complementary

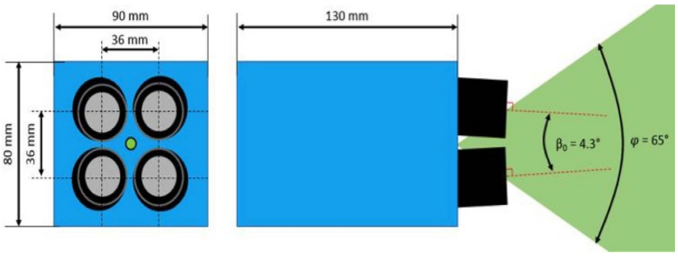

Figure 6. Schematic configuration of a coaxial volumetric velocimeter (repr. from Schneiders *et al* 2018).

Figure 7. Principle of particle trajectory measurement with CVV, with indication of axial (z) data dispersion due to small aperture.

metal-oxide-semiconductor) cameras with recording rate up to 1 kHz are utilized to allow the measurement of tracers' motion in time-resolved mode for flows at moderate speed (up to 15 m s^{-1}). At higher flow velocity, double-frame recordings are produced, however with a significant reduction in the accuracy of the velocity measurements. The shortcoming of the small angle subtended by the lines of sight is that the measurement of particle position and velocity along the axial direction is significantly poorer than along the other directions (figure 6). This condition is shared by other systems with small aperture, like digital holographic PIV (Meng *et al* 2004) and astigmatism PTV (Cierpka *et al* 2011).

A compact CVV system has been realized within approximately $10 \times 10 \times 15$ cm^3. Four cameras are placed at the corners of a square and a laser beam expands from the center of the front plate. The laser light is transported through optical fiber and expands conically with an angle of 65°.

The data analysis is based on detection and tracking of individual particle trajectories commonly done with 3D PTV algorithms (figure 7). In this case, an advanced algorithm performing Lagrangian particle tracking is adopted, given its robustness to densely seeded recordings and its intrinsic accuracy. The shake-the-box technique (STB, Schanz *et al* 2016) is based on the iterative particle reconstruction technique (Wieneke 2013) coupled with prediction and correction of particle images along individual trajectories. The resulting analysis is several orders of magnitude less computationally intensive than the procedure needed for tomographic reconstruction and 3D cross-correlation analysis.

Finally, the practical, yet not less important, task of maneuvering the measurement system needs to be accomplished by an automated device. The use of collaborative robots has been demonstrated in the recent work of Jux *et al* (2018a). Manipulation by robotic arm (figure 8) significantly expands the reach of the measurement system, typically attaining a (hemi)sphere of 2 m diameter.

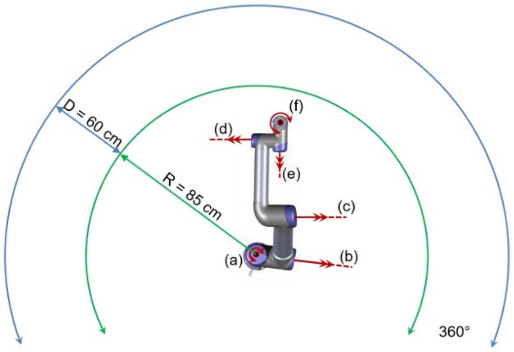

Figure 8. Measurement range of the coaxial volumetric velocimeter, operated from UR5 robotic arm.

3. Applications

The use of robotic PIV for large scale measurements has been demonstrated in several areas, from aeronautics to ground vehicle aerodynamics and speed sports. Two relevant applications are described here, namely the flow around a scaled turboprop aircraft and that around a full-scale cyclist.

3.1. Aircraft aerodynamics

Experiments are conducted in the low speed tunnel (LST) of the German-Dutch wind tunnels. The LST is a closed-loop closed-test-section wind tunnel, which features a contraction ratio of 9:1, a test section of 3×2.25 m^2, and a maximum free-stream velocity of 80 m s^{-1}. The wind tunnel model is a 1:12 scaled version of the EADS CASA C-295 aircraft, a twin-turboprop transport aircraft. The model is 1.97 m long; it has a wing span of 2.15 m, with 0.21 m mean chord. The model is connected to the LST six-components external balance held from the ceiling of the test section. The complete setup is shown in figure 9. The measurements are conducted at free-stream velocity of 8 and 50 m s^{-1}, with the aircraft in the take-off configuration at 9° angle of attack and the flaps deployed of 10°. The aircraft propeller is set at a rotating speed of 9600 rpm at free-stream velocity of 50 m s^{-1}, corresponding to a tip advance ratio of 0.96.

The flow around fuselage, wing and propeller is characterized with robotic PIV measurements spanning a volume of approximately $1.5 \times 1.0 \times 0.5$ m^3 with a mesh totaling approximately 10^6 measurement points.

The three-dimensional flow around the propeller and its interaction with the wing is shown in figure 10 with two cross sections selected past the propeller and downstream of the wing trailing edge. The momentum imparted by the propeller with initial axisymmetric distribution, is distorted by the adverse pressure gradient imposed at the wing leading edge (figure 10—left). Downstream of the wing, where the pressure gradient is assumed to have become negligible, the momentum distribution recovers more azimuthally homogeneous distribution (figure 10—right). An exception is the inward region, exhibiting visible momentum deficit, due to flow separation aside the nacelle.

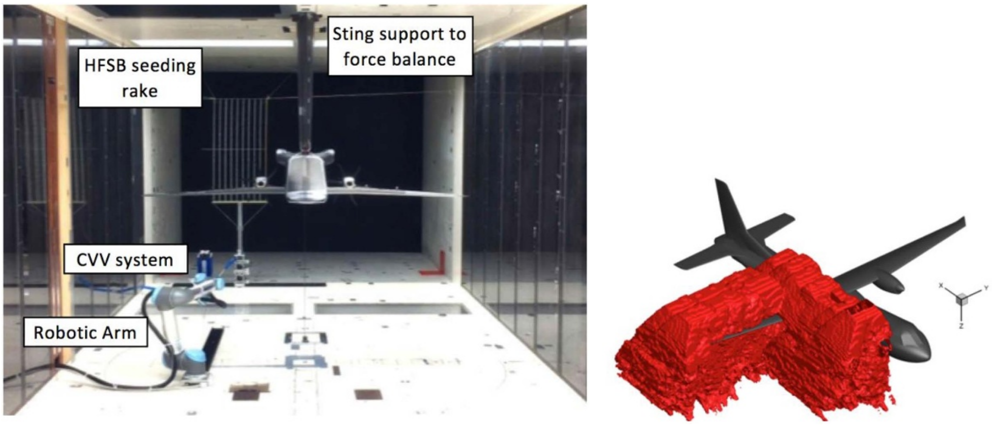

Figure 9. Left: layout of robotic PIV experiment in large aeronautical wind tunnel (view is from downstream the aircraft model). Right: measurement domain covered by CVV with robotic motion (repr. from Sciacchitano *et al* 2018).

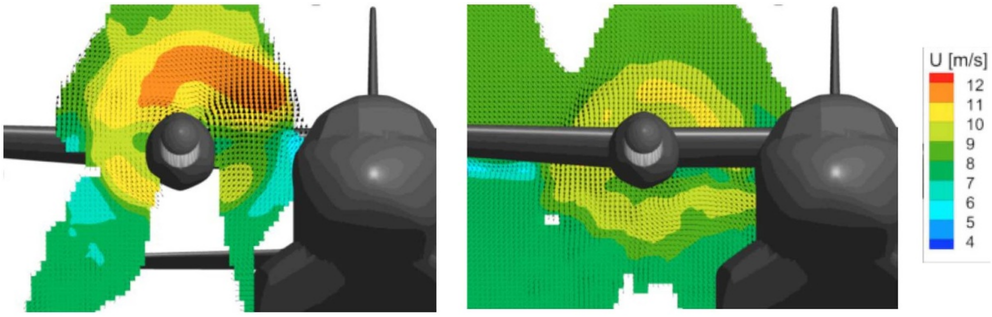

Figure 10. Time average velocity field at two cross sections (at propeller nacelle, left; past the wing, right). Streamwise velocity color contours and Y–Z-plane velocity vectors. Data from experiments at 8 m s^{-1} free stream velocity.

The streamwise component of the vorticity vector is examined in view of its relation with the formation and development of streamwise vortices at wing tips, flaps side edges and at nacelle-wing junctions. Figure 11 illustrates the three-dimensional structure of streamwise vortices, with two clockwise vortices emanating from the wing tip and the edge of the wing inner flap (color-coded in red). These vortices induce clockwise rotation of the flow (when observed from ahead of the aircraft) and they are due to the discontinuity in the lift distribution along the wingspan, specifically a drop outward. A streamwise vortex with opposite rotation (color-coded in blue) is observed to form at the inner side of the engine nacelle. Although, the nacelle, at flow incidence may produce a system of two counter-rotating vortices, only a single prominent vortex is observed. The latter is associated to the interaction between the flow swirl induced by the propeller (with counter-clockwise rotation) and the nacelle upper edge. As a result, a shear layer separates from the nacelle surface that rolls up into a vigorous vortex. The latter is also responsible for the localized loss of total pressure and momentum deficit downstream of the wing as discussed earlier for figure 10—right.

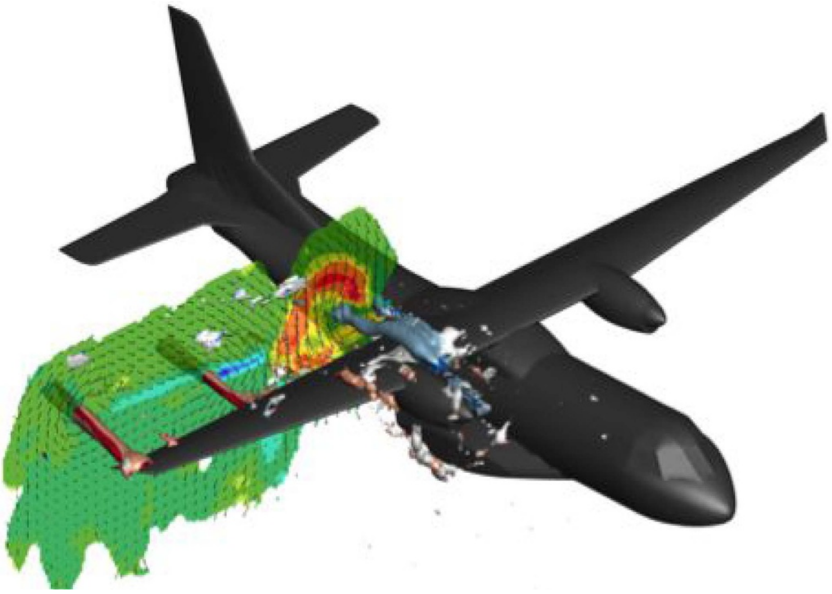

Figure 11. Visualization of streamwise vortices by Q-criterion iso-surfaces (color coding is based on streamwise vorticity). Cross section of velocity with color contours of streamwise component and vectors depicting the in-plane components (repr. from Sciacchitano *et al* 2018).

3.2. Cyclist aerodynamics at full scale

The detailed study of aerodynamic of sports is often hampered by the complexity of the human body, given its three-dimensional shape, motions and deformations during the sport action. Often, measurements are limited to determining the overall aerodynamic force, whereas the fluid dynamic processes at its source are investigated under simplified conditions with scaled models. Full scale aerodynamic analysis remains difficult with conventional planar PIV and wake flow survey can be conducted by pressure probes (Crouch *et al* 2014).

The complex flow around a full-scale replica of a professional cyclist has been mapped making use of robotic PIV. The athlete's body has been scanned for reproduction of a full-scale mannequin with 3D printing (figure 12). The mannequin is equipped with sport garments and installed on the race bicycle into the TU Delft Open Jet Facility at air speed of $U_\infty = 14$ m s^{-1} (figure 13). The measurement is built from more than 400 independent views taken at a rate of approximately 2 min each. The measurements comprise approximately 20×10^6 grid points distributed over a domain of $2.0 \times 1.6 \times 0.7$ m^3 (figure 14). Three-dimensional time averaged velocity and vorticity field around the athlete enable a detailed aerodynamic analysis to describe the distribution of sources of drag.

Figure 15 illustrates the flow field by velocity streamlines and color contours of the streamwise component in the median plane of the athlete. Flow stagnation at the helmet and at the steer is captured by the measurements. Acceleration along the athlete back curved in time-trial position is also evident. A large area of momentum deficit is observed in the wake of the athlete at the height of the hips as well as some localized deficit in the wake of the rear tire.

Much attention goes to the regions of flow separation. The iso-surface of streamwise velocity at $0.5\mathrm{U}_\infty$, respectively 7 m s^{-1}, indicates the areas where the flow is decelerated past the

Figure 12. Professional cyclist during sport action (left). 3D scan of the cyclist (middle). 3D printed replica for use in aerodynamic wind tunnel. (Permission for the inclusion of the Giant, Sunweb and Alpecin logos has not been sought. The inclusion of these logos is not intended to indicate any endorsement by, or collaboration with, the owners of the logos with this publication or any other IOP publishing material.)

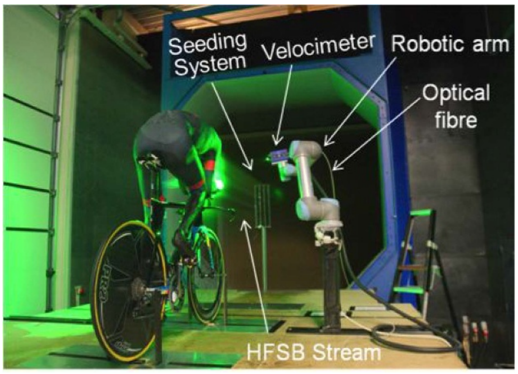

Figure 13. Layout of experiment (repr. from Jux *et al* 2018a).

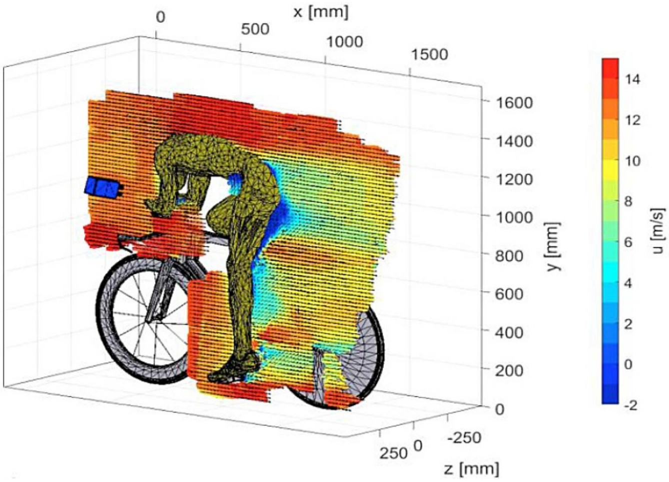

Figure 14. Illustration of the measurement domain scanning process with CVV, with one cross section of the time-average velocity field.

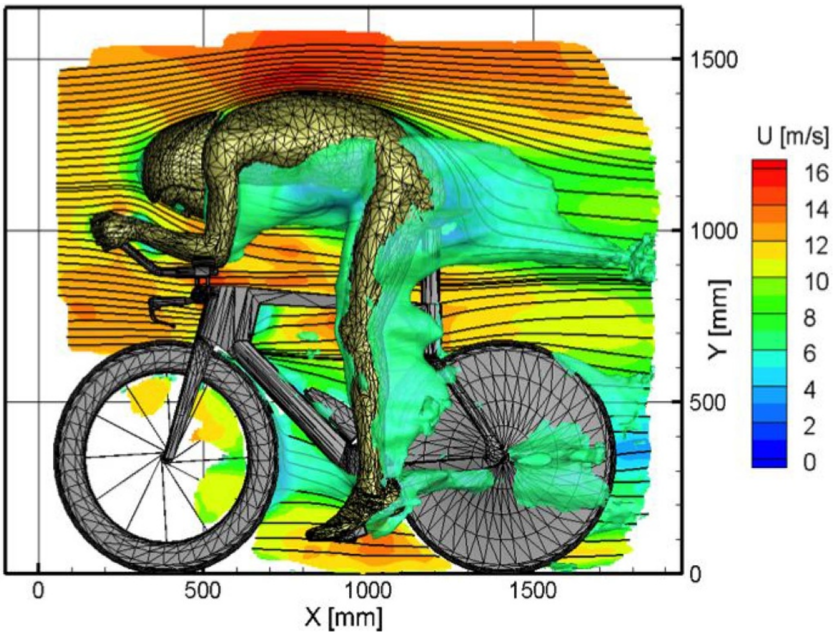

Figure 15. Time averaged velocity field around a full-scale cyclist model (repr. from Jux *et al* 2018a).

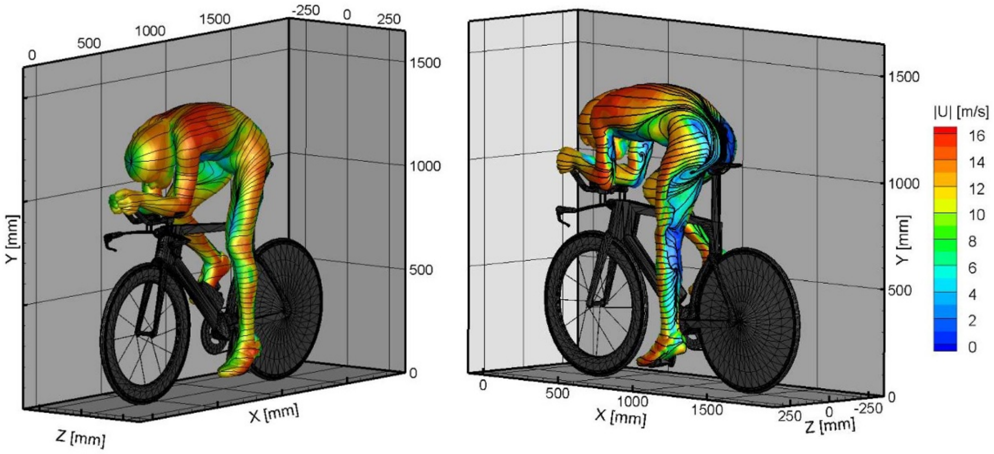

Figure 16. Near surface streamlines and color-coded streamwise velocity (repr. from Jux *et al* 2018a).

athlete, where flow separation potentially occurs. The iso-surface in figure 15 indicates a large region of flow deceleration in the complex enclosure between upper arms, breast and hips. The largest separation is presumably occurring from the lower back down to the upper leg. Also the flow around the stretched leg exhibits a wake, approximately scaling with the athlete's leg local cross section.

Table 1. Measurement features comparison for tomographic and robotic PIV.

	Tomographic PIV	Robotic PIV
Working fluid	Water Air and gases	Air
Velocity range	Up to supersonic speeds	Up to 70 m s^{-1}
Seeding	Micron droplets (2–5 part mm^{-3}) HFSB (2–5 part cm^{-3})	HFSB (<1 part cm^{-3})
Calibration	Target at three controlled positions + volume self-calibration (Wieneke 2008)	Factory calibration
Measured quantities	Instantaneous velocity	Instantaneous particle velocity
	Instantaneous velocity gradient	Time-avg. velocity and its gradient
	Velocity frequency spectrum (from time-resolved meas.)	Time avg. near-surface streamlines
Intrusivity	None	Robotic arm and CVV head unit
	From 10 to 200 cm^3	40 × 40 × 30 cm^3 (from single view)
Measurement domain	Thickness up to 2 cm	2 × 2 × 1 m^3 with robotic arm
	(several liters with HFSB)	
Spatial resolution	0.5–5 mm side correlation box	10–50 mm ensemble averaging bin
Accuracy	1%–2%	2% for u and v, 5% for w (axial component)
Number of recordings	100–500	5000–20 000
Computation time	~10 min/snapshot (based on 1 Mpx images)	~1 s/snapshot (using Shake-the-Box)

The three-dimensional pattern of streamlines, reduced in close proximity of the object surface, gives an indication of the skin-friction lines, which aids the interpretation of the near-surface flow behavior. Skin-friction lines are often produced by oil-flow visualization. The latter technique, however, cannot be easily applied on porous or absorbing surfaces such as the live athlete or its mannequin equipped with sport garments.

Figure 16 illustrates the pattern of the near-surface flow velocity. The stagnation point at the helmet is consistently captured by the streamlines topology as well as the velocity contours. A stagnation line is visible on the quasi-vertical body segments: upper arms and the stretched (left) leg (figure 16—left). The streamlines topology in the rear regions is more complex in nature, as it follows flow circulation induced by vortices and separated regions. Only the upper part of the upper arm seems to be affected by local flow separation (figure 16—left). The flow under the torso is redirected outwards, suggesting a separation line at the middle abdomen with formation of streamwise vortices. The main separation at the back appears to be rather limited to the region of glutei, connecting to the upper leg and extending down to the calves. No separation is inferred below the insertion between the calf and Achille’s tendon. Further details of the surface flow topology as well as visualizations of the surface pressure have been discussed in the recent works of Jux *et al* (2018b) and Schneiders *et al* (2018).

4. Measurement performance compared to 3D PIV

The following discussion summarizes the features measurement potential and limitations of robotic PIV compared to tomographic PIV, taken as a reference technique. From the data reported in table 1 it emerges clearly that, compared to tomographic PIV, the robotic PIV technique is not suited for the physical analysis of complex unsteady flows as it does not capture the unsteady organization of flow from the instantaneous velocity and vorticity field. Also, the typical resolution reached in robotic PIV experiments is of 1 vector cm^{-1}, opposed to 1 or more vectors mm^{-1} of tomographic PIV. A final limitation is the accuracy of the velocity component along the axial direction, considerably less than the other two components.

On the other hand, the robotic handling of the CVV system amplifies the maximum spatial range to more than a meter, the compact housing of cameras and illuminator make the calibration process unnecessary and the time for data processing is significantly less than for tomographic PIV, given the efficiency of the Lagrangian particle tracking algorithm STB.

5. Conclusions

The present survey illustrates the fundamental principles of robotic PIV for use in large-scale aerodynamics. The backbone of this technique is the use of helium filled soap bubbles, neutrally buoyant and in the sub-millimeter range. Such tracers can be detected with current lasers and cameras within a relatively large volume. However, the controlled production and distribution of these tracers in wind tunnels remains a subject that requires further developments.

The CVV is a device suited for the inspection of the flow from multiple directions, circumventing the problem of lengthy three-dimensional calibrations of cameras and illumination systems. The use of time-resolved recordings yields individual particle trajectories from which the velocity is obtained with high accuracy. The latter approach is needed to compensate the poor resolution of CVV along the axial direction caused by the small angular aperture of this compact system.

Two applications illustrate the current state-of-the-art of volumetric velocimetry for aerodynamics. The flow around a propeller aircraft is studied, yielding information on propeller wing and propeller-nacelle interactions. The aerodynamic analysis of a full-scale cyclist replica enables in-depth analysis of the flow around the athlete and in the near surface region. A good consistency is observed between momentum analysis and surface flow topology based on the near-surface streamlines.

Acknowledgments

The work presented herein is the result of fruitful collaborations among TU Delft and external partners. The support of the German-Dutch wind tunnel laboratories is acknowledged in giving access to the LST wind tunnel. LaVision GmbH has supported the development of coaxial volumetric velocimetry. The TU Delft Sport Engineering institute has supported the development of the 3D-printed replica of Tom Dumoulin.

References

Bosbach J, Kühn M and Wagner C 2009 Large scale particle image velocimetry with helium filled soap bubbles *Exp. Fluids* **46** 539–47

Bruecker C 1997 3D scanning PIV applied to an air flow in a motored engine using digital high-speed video *Meas. Sci. Technol.* **8** 1480–92

Caridi G C A, Ragni D, Sciacchitano A and Scarano F 2016 HFSB-seeding for large-scale tomographic PIV in wind tunnels *Exp. Fluids* **57** 190

Cierpka C, Rossi M, Segura R and Kähler C J 2011 On the calibration of astigmatism particle tracking velocimetry for microflows *Meas. Sci. Technol.* **22** 015401

Crouch T, Burton D, Brown N, Thompson M and Sheridan J 2014 Flow topology in the wake of a cyclist and its effect on aerodynamic drag *J. Fluid Mech.* **748** 5–35

Elsinga G E, Scarano F, Wieneke B and van Oudheusden B W 2006 Tomographic particle image velocimetry *Exp. Fluids* **41** 933–47

Engler Faleiros D, Tuinstra M, Sciacchitano A and Scarano F 2018 Helium-filled soap bubbles tracing fidelity in wall-bounded turbulence *Exp. Fluids* **59** 56

Jux C, Sciacchitano A and Scarano F 2018b Surface pressure visualization by 3D PIV *ISFV 18—Int. Symp. Flow Visualization* (*Zurich, Switzerland*) (https://doi.org/10.3929/ethz-b-000279192)

Jux C, Sciacchitano A, Schneiders J F G and Scarano F 2018a Robotic volumetric PIV of a full-scale cyclist *Exp. Fluids* **59** 74

Meng H, Pan G and Woodward S H 2004 Holographic particle image velocimetry: from film to digital recording *Meas. Sci. Technol.* **15** 673

Murai Y, Nakada T, Suzuki T and Yamamoto F 2007 Particle tracking velocimetry applied to estimate the pressure field around a Savonius turbine *Meas. Sci. Technol.* **18** 2491–503

Raffel M, Willert C E, Scarano F, Kaehler C J, Wereley S T and Kompenhans J 2018 *Particle Image Velocimetry—A Practical Guide* (Berlin: Springer)

Scarano F 2013 Tomographic PIV: principles and practice *Meas. Sci. Technol.* **24** 012001

Scarano F, Ghaemi S, Caridi G C A, Bosbach J, Dierksheide U and Sciacchitano A 2015 On the use of helium-filled soap bubbles for large-scale tomographic PIV in wind tunnel experiments *Exp. Fluids* **56** 42

Schanz D, Gesemann S and Schröder A 2016 Shake-the-box: Lagrangian particle tracking at high particle image densities *Exp. Fluids* **57** 70

Schneiders J F G, Scarano F, Jux C and Sciacchitano A 2018 Coaxial volumetric velocimetry *Meas. Sci. Technol.* **29** 065201

Sciacchitano A, Giaquinta D, Schneiders J F G, Scarano F, van Rooijen B and Funes D E 2018 Quantitative visualization of the flow around a turboprop aircraft model by robotic volumetric velocimetry *ISFV 18—Int. Symp. Flow Visualization* (*Zurich, Switzerland*) (https://doi.org/10.3929/ethz-b-000279206)

Tescione G, Ragni D, He C, Simão Ferreira C J and van Bussel G J W 2014 Near wake flow analysis of a vertical axis wind turbine by stereoscopic particle image velocimetry *Renew. Energy* **70** 47–61

Wieneke B 2008 Volume self-calibration for 3D particle image velocimetry *Exp. Fluids* **45** 549–56

Wieneke B 2013 Iterative reconstruction of volumetric particle distribution *Meas. Sci. Technol.* **24** 024008